

# Embedded Investigation of Synchronous Reluctance Motor Drive For Electric Two Wheeler

Jitendra Kumar Nama

*Research and Development*

*Electrical Research and Development Association*

Vadodara, India

asheesh.dhaneria@erda.org, jknama1000@gmail.com

**Abstract**—Achieving carbon net zero, a crucial goal for the electric vehicle (EV) industry, is hampered by the reliance on limited permanent magnet resources imported from abroad, which form the core of motor drives. To address this challenge, this paper explores the synchronous reluctance motor (SynRM) as a viable alternative. SynRM technology readily leverages existing manufacturing capabilities, offering a cost-effective solution. We investigate the performance of a 2.2 kW SynRM drive specifically designed for the EV two-wheeler industry. Based on extracted motor parameters, a mathematical model is developed to facilitate a thorough steady-state analysis of its performance characteristics. The model's accuracy is further validated through simulations conducted using MATLAB/Simulink software. Finally, a hardware prototype is designed and implemented using a Texas Instruments DSP TMS320F28335 to verify the theoretical and simulated findings.

**Index Terms**—Synchronous reluctance motor (SynRM) drive, Electric drive, MTPA.

## I. INTRODUCTION

The promise of independent production of electric vehicle (EV) for India's micro, small and medium-sized enterprises (MSMEs) is encouraged by the synchronous reluctance motor (SynRM) [1]. Its advantages shine in comparison to both induction motors (IMs) and brushless DC (BLDC) motors. SynRMs boast higher stiffness, require less copper, and incur lower costs due to the absence of permanent magnets or rare earth materials [2]. These attributes have driven their recent adoption in the drive, fan, and pump industries, where their simple design, ease of control, and high productivity have proven advantageous. The burgeoning electric vehicle (EV) industry is also taking notice, with SynRMs emerging as a compelling alternative due to the escalating cost and limited availability of rare earth materials. Despite its potential, SynRM adoption in the EV market necessitates a firmer foundation. Further development is crucial to solidify its position in this demanding sector.

The fundamental principle of the reluctance motor is based on the interaction between magnetic flux lines and iron-core components. When a ferrous metal piece is placed within a magnetic field, it induces magnetic poles on the metal piece, creating attractive or repulsive forces with the source of the magnetic field. If a point on the metal piece is fixed for rotation (as in the rotor of a motor), mechanical forces arise between

it and the source magnet. Both elements strive to achieve a minimum reluctance path for the flux lines, resulting in generating the required torque [3].

The existing literature presents various inverter topologies for shaping the generated torque in electric vehicles (EVs) to suit their specific application needs. These include voltage source inverters with three-phase two-level, multilevel, four-switch, and eight-switch configurations. For a smooth and comfortable driving experience, EVs require ripple-free load and electrical torque [3]. However, two-wheelers face stricter space and weight constraints, necessitating high tolerance limits for their EV applications.

To address the space limitations, three-phase two-level inverters with either six or four switches can be considered [4]. However, the four-switch topology presents challenges in the form of increased control complexity and reduced capacitor lifespan, making it less suitable for two-wheelers [4]. To overcome these limitations and enable regenerative braking, a boost-fed two-level inverter topology has been proposed [5]. However, the boost converter limits voltage amplification from the DC battery, requiring a larger and higher voltage battery, which is undesirable for the chosen EV application.

To improve voltage gain and provide galvanic isolation between the low-voltage battery and the high DC link voltage, a transformer-based DC-to-DC converter topology can be selected. Notably, the drive topologies presented in references [3] - [5] are not designed for operation in the field weakening region. The author in reference [6] proposes a control methodology to enable operation beyond the nominal drive speed. Inspired by the reviewed literature, a drive system was developed in the laboratory using a Texas Instruments TMS320F28335 DSP [7] and [8], with code optimization performed within the CCS IDE.

This article is structured as follows. Section II explores the different topologies available for implementing the SynRM drive and justifies the chosen configuration based on its suitability for the EV application. Section III describes the mathematical modeling of the key components of the drive system, including the primary DC-to-DC converter, the main inverter, and the SynRM motor. Section IV details the embedded code development process for the Texas Instrument's digital signal processor (DSP) TMS320F28335 experimenter's kit's using Code Composer Studio (CCS) integrated development envi-

Sponsored by Electrical Research and Development Association

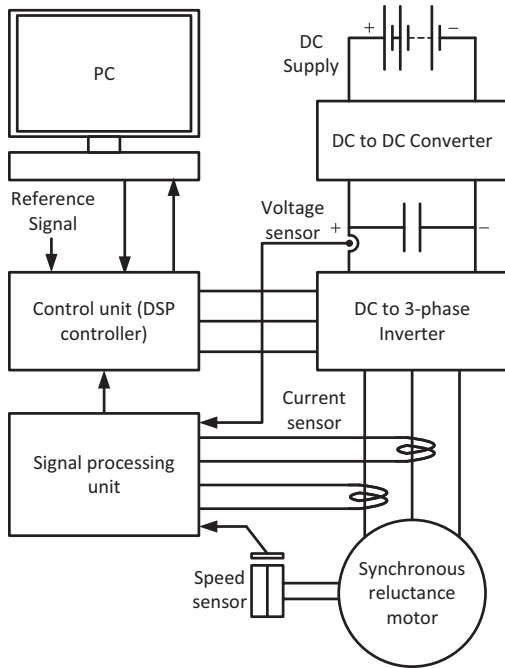


Fig. 1. Generic arrangement of sensed SynRm drive

ronment. The code will implement the control algorithms for the drive system based on the developed mathematical models. Section V presents and analyzes the simulation and hardware results, while Section VI summarizes the key findings of the article, highlights the contributions made, and potentially suggests future research directions in the field.

## II. TOPOLOGY SELECTION

The selection of the drive topology is paramount to the performance of the entire system. It defines the power electronic components and their interconnection, ultimately dictating the efficiency, controllability, and cost of the drive. Fig. 1 provides a schematic representation of a typical drive system, illustrating the systematic arrangement of its general hardware components.

### A. Motor Selection

This study investigates the performance of synchronous reluctance motors (SynRMs) for electric vehicle (EV) applications. Focusing on a specific case study, we analyze a 2.2 kW, 440 V, 50 Hz, delta-connected SynRM developed by the Electrical Research and Development Association (ERDA) for two-wheeler EVs. SynRM operation relies on the principle of variable reluctance, introduced by its unique rotor design. A wide variety of geometrical shapes are possible for SynRM rotors, and this study focuses on the transversally laminated design depicted in fig. 2. This specific design is chosen to minimize iron losses and enhance the rotor's saliency ratio, thereby improving overall motor efficiency. The performance characteristics of the selected rotor design are then imported

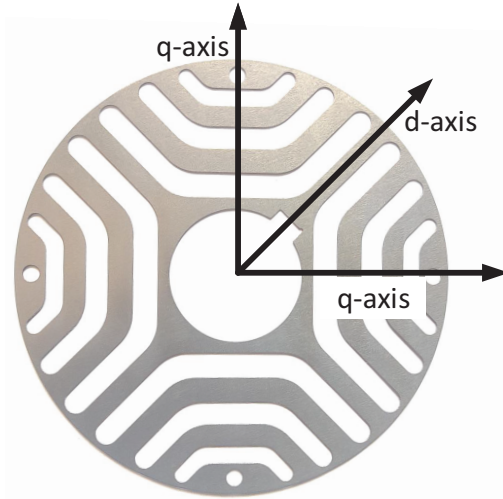


Fig. 2. SynRM's transversally laminated anisotropic (TLA) rotor sheet designed by ERDA

into Ansys Maxwell for finite element analysis. It is important to note that the chosen SynRM shares a similar stator configuration with an induction motor, employing distributed three-phase windings to generate a rotating magnetic field.

### B. Power Electronic Converters Selection

This section focuses on selecting an inverter topology to convert the DC input power into a three-phase AC supply suitable for driving the chosen motor. The motor's delta-connected stator winding necessitates a three-phase, three-wire inverter configuration. Additionally, the inverter must operate with pulse-width modulation (PWM) that minimizes third harmonic components, similar to sine PWM. Furthermore, the control scheme needs to ensure minimal current error even with the present line inductance. Considering these requirements, a three-phase, two-level inverter emerges as the most suitable option due to its minimal component cost and relatively straightforward implementation using the chosen DSP controller.

The chosen three-phase inverter necessitates a high-voltage DC supply exceeding the capabilities of the current two-wheeler EV battery (72V). Therefore, a voltage boost converter becomes necessary to increase the battery voltage to required value, the operating requirement of the inverter. Literature suggests that a push-pull converter with a 1:10 transformer turn ratio offers the most compact configuration while delivering sufficient voltage boost for the selected motor rating.

The adopted DC-DC converter employs an independent control scheme to regulate the DC link voltage  $V_{Ca}$  and ensure sufficient capacity for both input ripple filtering and transient demands of the inverter. This control scheme eliminates the need for an additional filter at the inverter output due to the inherent inductance of the motor. Consequently, the major components for the drive system are selected as the DC-DC

converter, the three-phase, two-level inverter, and the SynRM motor.

### III. MATHEMATICAL MODEL DEVELOPMENT

Designing a successful variable frequency drive demands a comprehensive understanding of both individual and combined component operation. For SynRM drives, the key principle lies in minimizing magnetic flux path resistance by adjusting the position of metal elements within the rotor. The stator design, resembling that of an induction motor, employs distributed three-phase windings to generate the requisite magnetic field. A specially designed rotor, adhering to the variable reluctance principle, is mounted on the stator shaft for free rotation.

Effective field-oriented speed control requires the transformation of existing three-phase currents, voltages, and impedances into two-phase direct-axis (d-axis) and quadrature-axis (q-axis) parameters. While the literature presents five standard control strategies for SynRM speed control, the maximum torque per ampere (MTPA) method proves advantageous due to its simplicity and stable operation. Building upon a generic SynRM model, this study develops a bespoke mathematical model to serve as the bedrock for understanding and planning the control scheme. (1) and (2) subsequently define the relationship between the drive's input voltage, current, and the d-q plane.

$$v_{ds} = R_s i_{ds} + L_{ds} \frac{di_{ds}}{dt} - P\omega_s \lambda_{qs} \quad (1)$$

$$v_{qs} = R_s i_{qs} + L_{qs} \frac{di_{qs}}{dt} + P\omega_s \lambda_{ds} \quad (2)$$

The d-q axis model is represented by (1) and (2), where lowercase subscripts denote *d-axis* and *q-axis* quantities and uppercase subscripts represent stator parameters. The  $v_{ds}$  and  $v_{qs}$  are the stator voltages,  $i_{ds}$  and  $i_{qs}$  are the stator currents,  $\lambda_{ds}$  and  $\lambda_{qs}$  are the stator flux linkages, and  $L_{ds}$  and  $L_{qs}$  are the stator inductances. The angular electrical rotor speed is denoted by  $\omega_s$ ,  $P$  is the number of pole pairs, and  $R_s$  is the stator resistance. All parameters are expressed in SI units.

The electromagnetic torque  $T_{elect}$  is defined as

$$T_{elect} = \frac{3}{2}P(\lambda_{ds}i_{qm} - \lambda_{qs}i_{dm}) \quad (3)$$

Here the factor  $\frac{3}{2}$  arises from the three-phase system and  $P$  accounts for the pole pair number. The torque depends on the interaction between the *d-axis* and *q-axis* components of stator current ( $i_{dm}$  and  $i_{qm}$ ) and *d-axis* and *q-axis* stator flux linkages ( $\lambda_{ds}$  and  $\lambda_{qs}$ ).

Where,  $T_{elect}$  supplies the load torque and acceleration requirement as shown in 4.

$$T_{elect} = T_{mech} + \frac{J_{eq}}{P} \times \frac{d\omega_s}{dt} + \frac{B\omega_{eq}}{P} \times \omega_s \quad (4)$$

Equation (4) explicitly connects the electromagnetic torque  $T_{elect}$  to the mechanical requirements of the system.  $T_{mech}$ , representing the load torque, specifies the external resistance the motor needs to overcome.  $J_{eq}$ , the combined moment

of inertia of the machine and load, determines how readily the system accelerates or decelerates in response to torque variations.  $B_{eq}$ , the combined friction coefficient, accounts for the internal energy losses due to friction within the machine and between it and the load.

Equations (1) and (2) provide the basis for extracting and processing the machine current. This is achieved through the current sensor, adhering to the requirements of the DSP's analog-to-digital converter (ADC) module. Similarly, rotor speed is measured using the ADC in conjunction with an encoder, enabling the implementation of the speed control loop.

### IV. EMBEDDED CONTROL ALGORITHM DEVELOPMENT

Precise speed control with minimal hardware complexity is paramount for electric vehicle (EV) drive systems. In vehicle applications, accurate speed feedback is readily available from the speedometer, therefore, a sensor-based control scheme is adopted. This approach, combined with field-oriented control, allows for precise speed control while avoiding unnecessary torque control complexity. Large torque ripple associated with torque-centric control methods could induce unwanted vehicle vibrations and compromise ride quality. Therefore, a sensor-based field-oriented control scheme, as illustrated in the fig. 3, is chosen for the presented EV drive system.

The proposed system's control process begins with a reference speed command provided by the driver interface. Commercially available accelerometers, typically requiring a 5V input, generate an analog or PWM signal for speed reference. This signal undergoes pre-processing by a low-pass filter to attenuate any ripple content and introduce a desired delay. Following preprocessing, the signal is fed to the DSP's ADC pin as the speed reference. Feedback on the actual vehicle speed is obtained from either the vehicle's speedometer or a dedicated speed encoder and then fed into the DSP's QEP pins. These pins connect to the QEP module, which generates the current angular position and direction of the vehicle. Comparing the reference and feedback speeds generates an error signal, which is subsequently processed by a PI controller to produce the reference torque signal. This marks the initiation of the primary control operation for the SynRM motor. In literature there are following control schemes are discussed as

- Maximum torque per ampere control (MTPAC)
- Maximum rate of change of torque control (MRCTC)
- Maximum power factor control (MPFC)
- Constant current in the inductive axis control (CCIAC)
- Field weakening control (FWC)

The embedded code implements the Maximum Torque per Ampere (MTPA) control scheme, aptly named for its ability to maximize torque output for each unit of current. This approach facilitates the straightforward calculation of the direct-axis ( $i_{ds}$ ) and quadrature-axis ( $i_{qs}$ ) current references using (3) within the DSP. By exploiting the relationships between flux linkages and currents ( $\lambda_{ds} = L_{ds}i_{ds}$  and  $\lambda_{qs} = L_{qs}i_{qs}$ ), (3) can be rewritten as the simplified form shown in (5).

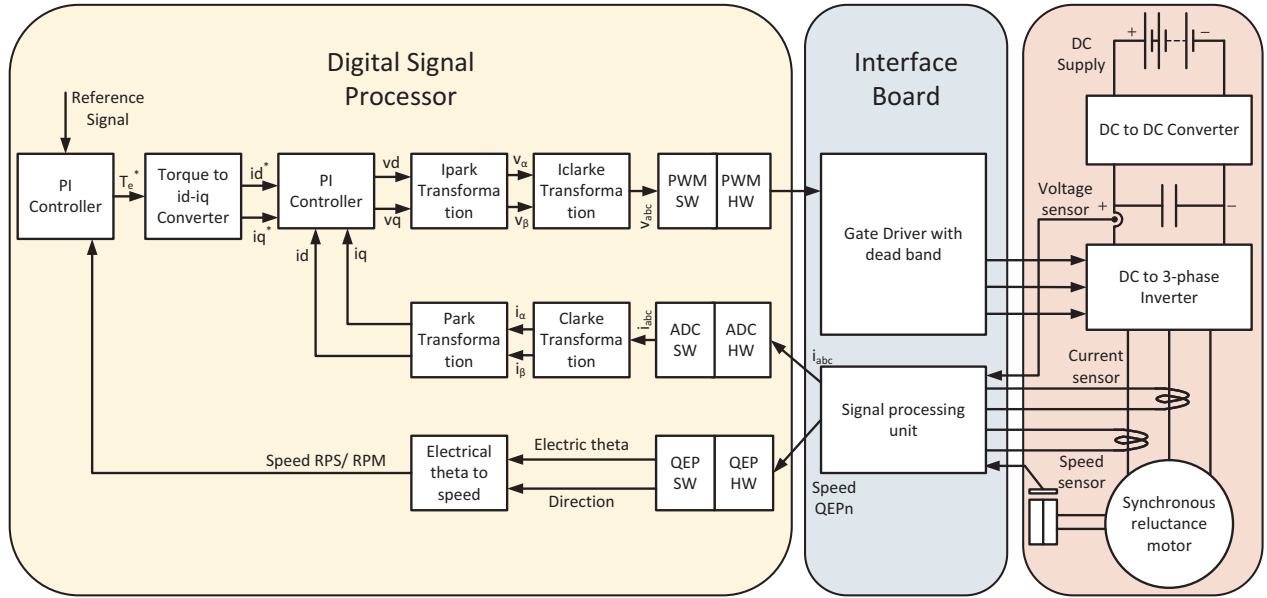


Fig. 3. Embedded implementation strategy for SynRm drive

Differentiating (5) and substituting the constraint imposed by the total stator current squared ( $i_s^2 = i_{ds}^2 + i_{qs}^2$ ) allows for the determination of the maximum achievable torque. Notably, setting  $i_{ds} = i_{qs}$  in (5) leads to the specific expression for maximum torque, as shown in (6).

$$T_{elect} = \frac{3}{2} \left( \frac{P}{2} \right) (L_{ds} - L_{qs}) i_{ds} i_{qs} \quad (5)$$

$$T_{elect(max)} = \frac{3}{2} \left( \frac{P}{2} \right) (L_{ds} - L_{qs}) \left( \frac{i_s}{\sqrt{2}} \right) \quad (6)$$

These references are then compared with the actual currents,  $i_d$  and  $i_q$ , extracted from the three-phase currents ( $i_{abc}$ ) using Clarke and Park transformations.

The Park transformation first converts the  $i_{abc}$  quantities to a two-phase orthogonal  $\alpha - \beta$  domain. Subsequently, the Clarke transformation further translates these into the desired synchronous rotating  $d-q$  domain, representing direct-axis and quadrature-axis components. This conversion to DC quantities is crucial for processing within the DSP.

The error generated by comparing the reference and actual  $d-q$  currents feeds into a PI controller, generating a voltage reference. This reference is then inverted through inverse Clarke (iClarke) and inverse Park (iPark) transformations to obtain the three-phase voltage signals ( $v_{abc}$ ). Finally, the PWM module generates the corresponding pulse-width modulated signals for driving the inverter.

The specific equations for the Clarke (for  $\alpha-\beta$  to  $d-q$  frame), iClarke (for  $d-q$  to  $\alpha-\beta$  frame), Park (for  $a-b-c$  to  $\alpha-\beta$  frame), and iPark (for  $\alpha-\beta$  to  $a-b-c$  frame) transformations are provided by (7), (8), (9), and (10) respectively.

$$\begin{bmatrix} v_d \\ v_q \\ v_0 \end{bmatrix} = \begin{bmatrix} \cos(\omega t) & \sin(\omega t) & 0 \\ -\sin(\omega t) & \cos(\omega t) & 0 \\ 0 & 0 & 0 \end{bmatrix} \times \begin{bmatrix} v_\alpha \\ v_\beta \\ 1 \end{bmatrix} \quad (7)$$

$$\begin{bmatrix} v_\alpha \\ v_\beta \\ 1 \end{bmatrix} = \begin{bmatrix} \cos(\omega t) & -\sin(\omega t) & 0 \\ \sin(\omega t) & \cos(\omega t) & 0 \\ 0 & 0 & 0 \end{bmatrix} \times \begin{bmatrix} v_d \\ v_q \\ v_0 \end{bmatrix} \quad (8)$$

$$\begin{bmatrix} v_\alpha \\ v_\beta \\ 1 \end{bmatrix} = \begin{bmatrix} \frac{2}{3} & -\frac{1}{3} & -\frac{1}{3} \\ 0 & \frac{1}{\sqrt{3}} & -\frac{1}{\sqrt{3}} \\ \frac{1}{3} & \frac{1}{3} & \frac{1}{3} \end{bmatrix} \times \begin{bmatrix} v_a \\ v_b \\ v_c \end{bmatrix} \quad (9)$$

$$\begin{bmatrix} v_a \\ v_b \\ v_c \end{bmatrix} = \begin{bmatrix} 1 & 0 & 1 \\ -\frac{1}{2} & \frac{\sqrt{3}}{2} & 1 \\ -\frac{1}{2} & -\frac{\sqrt{3}}{2} & 1 \end{bmatrix} \times \begin{bmatrix} v_\alpha \\ v_\beta \\ 1 \end{bmatrix} \quad (10)$$

## V. RESULTS AND DISCUSSION

Building upon the presented analysis, the proposed system's mathematical model is further refined. Through experimental procedures such as blocked-rotor, continuous running, and loading tests, the values of the d-axis and q-axis inductances ( $L_d$  and  $L_q$ ) are accurately identified. These measured values are subsequently incorporated into the analysis to develop a comprehensive simulation model within the MATLAB/Simulink environment.

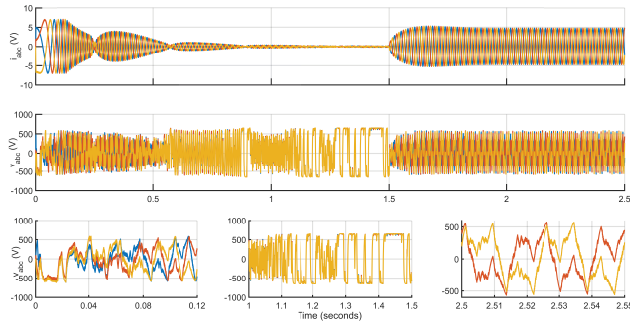


Fig. 4. Speed response of SynRM drive with hysteresis controller.

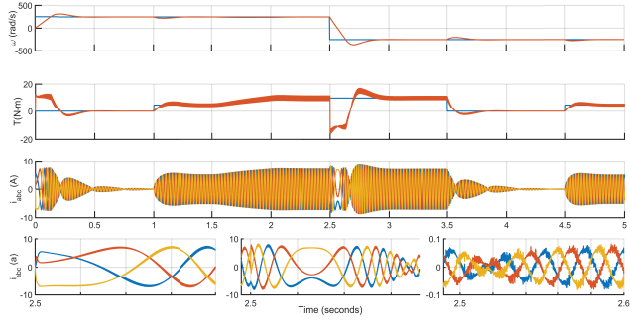


Fig. 5. Speed response of SynRM drive with PI controller.

### A. Simulation Results

Leveraging the control system design outlined in Section IV, the simulation is then utilized to evaluate the system's performance, with the key results showcased in fig. 4 and 5.

Figure 4 presents the implementation of the MTPA scheme with a hysteresis current controller. This approach simplifies PI tuning by enabling the substitution of individual PI current controllers with a single PI torque controller. However, while the motor currents remain sinusoidal as expected, the three-phase voltages exhibit a significant deviation from pure sinusoidal waveforms. Notably, the voltage differences ( $v_{ab}$ ,  $v_{bc}$ ,  $v_{ca}$ ) maintain a sinusoidal character, but a non-zero DC component is evident in the voltage waveforms. This DC component raises concerns about potential motor flux saturation or rotor blocking under certain operating conditions. To mitigate this risk and ensure smooth operation, the introduction of a dedicated PI voltage controller is used in fig. 5.

The implementation of a PI voltage controller effectively eliminates the zero-sequence component in the output three-phase voltage. This strategic control choice allows for the removal of voltage sensors from the inverter output circuit. Consequently, during the product development stage, a single voltage sensor at the DC bus suffices, ensuring the proper operation of both the primary DC/DC converter and the drive inverter.

Figure 5 showcases the SynRM drive's performance under various loading conditions, with expanded views for startup, reversal, and no-load scenarios. As predicted by (5) and (6)

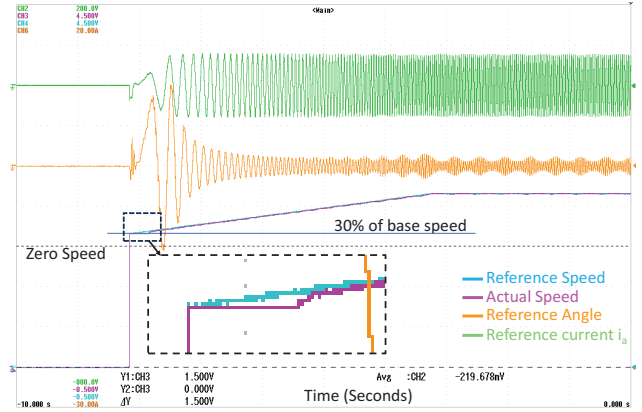


Fig. 6. Speed response of SynRM drive.

from fig. 3, the maximum speed error at standstill generates the maximum torque, resulting in the highest allowable current. However, at standstill and low speeds, the motor's back-emf is low, leading to correspondingly low voltage and limited current, effectively supplying only current and power for frictional and windage losses. Table 1 details the motor parameters. Fig. 5 demonstrates that the speed remains constant under varying load demands, with the controller appropriately adjusting the electromagnetic torque to meet these demands. For smooth torque increases, the current rises gradually, and during a speed reversal command, the current phase sequence changes to adapt to the reversed torque direction.

### B. Hardware Implementation

To experimentally validate the developed SynRM model and its simulation findings, a laboratory prototype was constructed. During component selection, careful consideration was given to accurately replicate real-world operating conditions. Table 1 specifies the components employed in the prototype. Notably, the prototype incorporates a soft-start mechanism for the SynRM motor, and the resulting performance is showcased in fig. 6.

The experimental results demonstrate the developed controller's ability to provide the necessary starting torque and maintain synchronous operation. During motor startup, a slight delay is deliberately introduced to facilitate the minimum required flux buildup for rotor lock-on with the rotating magnetic field. As the motor accelerates, the speed feedback loop engages, driving the error towards zero and enabling precise speed tracking. The presented results showcase the motor operating at 125% of its base speed within the flux weakening region, exhibiting smooth response and minimal ripple in the output.

## VI. CONCLUSION

This paper investigates the Synchronous Reluctance Motor (SynRM) as a potential alternative to permanent magnet-based motor drives, particularly for two-wheeler applications. A specific SynRM developed by ERDA is analyzed and tested,

TABLE I  
SPECIFICATION OF HARDWARE COMPONENTS

Specifications	Part No.
Push-Pull Power MOSFET	IXFT120N30X3HV
Rectifier diode	VS-E5TH1512S2LHM3
Gate driver IC	TC4420, TC4429
Power inverter IGBT	SKM75GB12T4
Gate driver	SKYPER 32 R
Current sensor	LXSR-6-NPS
DC link voltage sensor	DVC 1000-P
Encoder	FNC 100H32630V1024-R7
DSP Controller	LUNCHXL F28335
Lithium-Ion	72V 100Ah
SynRM Motor	2.2kW, 4.5A, 1500rpm
Measured $R_s$ , $L_d$ , $L_q$	1.43 $\Omega$ , 0.306H, 0.0858H
Measured $J$ , $B_m$ ,	0.00582 $kg - m^2$ , 0.00035

and a mathematical model is constructed to enable various simulated experiments. Subsequently, a laboratory prototype was developed, equipped with a fully digitized Maximum Torque per Ampere (MTPA) control scheme implemented on a TMS320F28335 DSP using CCS IDE. This scheme incorporates a soft-start feature to ensure smooth operation during motor startup. Extensive tests, including drive starting and steady-state operation, were conducted to verify the suitability of the SynRM for electric vehicle (EV) applications. The results obtained successfully validate the proposed approach. Future work will focus on conducting IEC standardized tests on the drive to ensure it meets industry requirements and standards.

#### REFERENCES

- [1] H. El Hadraoui, M. Zegrari, A. Chebak, O. Laayati, and N. Guennouni, "A multi-criteria analysis and trends of electric motors for electric vehicles," *World Electric Vehicle Journal*, vol. 13, no. 4, 2022. [Online]. Available: <https://www.mdpi.com/2032-6653/13/4/65>
- [2] H. Heidari, A. Rassölkin, A. Kallaste, T. Vaimann, E. Andriushchenko, A. Belahcen, and D. V. Lukichev, "A review of synchronous motor-drive advancements," *Sustainability*, vol. 13, no. 2, 2021. [Online]. Available: <https://www.mdpi.com/2071-1050/13/2/729>
- [3] X. Dianguo, J. Xinhai, and C. Wei, "Sensorless control of synchronous reluctance motors," in *2017 IEEE Transportation Electrification Conference and Expo, Asia-Pacific (ITEC Asia-Pacific)*, 2017, pp. 1–4.
- [4] C.-K. Lin and C. A. Agustin, "Hybrid switching of four-voltage-vector model-free predictive current control for four-switch three-phase inverter-fed synrm drive systems," *IEEE Open Journal of the Industrial Electronics Society*, vol. 3, pp. 537–550, 2022.
- [5] G. V. Kumar, C.-H. Chuang, M.-Z. Lu, and C.-M. Liaw, "Development of an electric vehicle synchronous reluctance motor drive," *IEEE Transactions on Vehicular Technology*, vol. 69, no. 5, pp. 5012–5024, 2020.
- [6] A. Credo, M. Villani, G. Fabri, and M. Popescu, "Adoption of the synchronous reluctance motor in electric vehicles: A focus on the flux weakening capability," *IEEE Transactions on Transportation Electrification*, vol. 9, no. 1, pp. 805–818, 2023.
- [7] M. Bhardwaj, "Sensorless field oriented control of 3-phase induction motors using f2833x," *Texas Instruments, Application Report SPRABQ0*, 2013.
- [8] R. T. Ramamoorthy, B. Larimore, and M. Bhardwaj, "Sensored field oriented control of 3-phase permanent magnet synchronous motors using tms320f2837x," *Texas Instruments, Application Report, SPRZBZ0*, (Feb. 2016), vol. 39, 2016.